

# A Letter-of-Intent to Jefferson Lab PAC52

## Measurement of the Two-Photon Exchange Contribution to the Positron-Neutron Elastic Scattering Cross Section

E. Fuchey (spokesperson), D. Armstrong, T. Averett, M. Satnik, and Z. Wertz

*The College of William and Mary, Williamsburg, Virginia 23185, USA*

S. Alsalmi (spokesperson)

*King Saud University, Riyadh 11451, Saudi Arabia*

C. Ayerbe Gayoso

*Old Dominion University, Norfolk, Virginia 23529, USA*

J. Boyd, N. Liyanage, and M. Rathnayake

*University of Virginia, Charlottesville, Virginia 232904, USA*

P. Datta, A.J.R. Puckett, and S. Seeds

*University of Connecticut, Storrs, Connecticut 06269, USA*

R. Montgomery

*SUPA School of Physics and Astronomy,*

*University of Glasgow, Glasgow G12 8QQ, UK*

A. Tadepalli

*Thomas Jefferson National Accelerator Facility, Newport News, Virginia 23606, USA*

(Dated: April 17, 2024)

## Abstract

We propose to make a high precision measurement of the two-photon exchange contribution (TPE) in elastic positron-neutron scattering at two four-momentum transfers  $Q^2$  of 3.0 and 4.5  $GeV^2$ . This measurement purports to complete and extend the measurement of the two-photon exchange in electron-neutron scattering submitted to and approved by PAC48 in 2020, and recorded in 2022 (experiment E12-20-010, currently under analysis), which was the first experiment to examine the impact of the TPE in the neutron form factors experimentally. This program means to address the open question of the discrepancy between GE /GM ratios measured in elastic electron-nucleon scattering via Rosenbluth separation on the one-hand and polarization transfer on the other hand, with the former known to be sensitive to the TPE contribution while the latter isn't. The comparison between the Rosenbluth slope in the positron-neutron measured by the proposed experiment and the Rosenbluth slope in electron-neutron measured by E12-20-010 will provide significant insight on the TPE contribution in the neutron form factors, completing the efforts of MUSE at PSI and the proposed E12+23-008 to measure the TPE contribution on the proton form factors.

The proposed experiment shall be performed in Hall A and will measure simultaneous positron-proton and positron-neutron scattering off deuterium, extracting the Rosenbluth slope of positron-neutron quasi-elastic scattering at two beam energies of 3.3 and 4.4 GeV for  $Q^2 = 3.0\text{ }GeV^2$ , and 4.4 and 6.6 GeV for  $Q^2 = 4.5\text{ }GeV^2$ . In the proposed approach, systematic errors for positron neutron scattering are greatly reduced compared to those in the traditional single arm configuration. The experimental setup of the proposed experiment will be identical to that of the E12-20-010 experiment, using the BigBite (BB) spectrometer to detect the scattered positrons and the Super BigBite Spectrometer (SBS) to detect the protons and neutrons, combined with the proposed positron beam-upgrade for CEBAF. Using the maximum proposed intensity of 1  $\mu\text{A}$  unpolarized positrons on 15 cm cryogenic deuterium target, this measurement requires 8 days on both kinematics. In addition, the measurement requires two extra day with electron beams and 15 cm cryogenic hydrogen and deuterium target (with 10  $\mu\text{A}$  intensity) for calibrations and nucleon detection efficiency measurements, plus two extra days for kinematic change. The analysis of the proposed

experiment will greatly benefit on the return of experience of the ongoing analysis of E12-20-010.

## I. INTRODUCTION

In 1950s, a series of experiments performed by R. Hofstadter [1] revealed that nucleons have a substructure (which corresponds to our modern view in terms of quarks and gluons). The experiment confirmed M. Rosenbluth's theory of electron scattering [2] based on the one-photon exchange approximation. In this so-called Born approximation, where the interaction between the electron and the nucleon occurs *via* an exchange of one virtual photon (OPE), the unpolarized  $e - N$  elastic cross section can be parameterized in terms of a nucleon magnetic,  $G_M$ , and electric,  $G_E$ , form factors. These form factors describe the deviation from a point-like scattering cross section,  $\sigma_{Mott}$ :

$$\left( \frac{d\sigma}{d\Omega} \right)_{eN \rightarrow eN} = \frac{\sigma_{Mott}}{\epsilon(1 + \tau)} [\tau \cdot G_M^2(Q^2) + \epsilon \cdot G_E^2(Q^2)], \quad (1)$$

where  $E$  and  $E'$  are the incident and scattered electron energies, respectively,  $\theta$  is the electron scattering angle,  $\tau \equiv -q^2/4M^2$ , with  $-q^2 \equiv Q^2 = 4EE' \sin(\theta/2)$  being the negative four momentum transfer squared,  $M$  is the nucleon mass, and  $\epsilon = [1 + 2(1 + \tau) \tan^2(\theta/2)]^{-1}$  is the longitudinal polarization of the virtual photon. The reduced cross section is defined by:

$$\sigma_r \equiv \left( \frac{d\sigma}{d\Omega} \right) \cdot \frac{\epsilon(1 + \tau)}{\sigma_{Mott}} = \tau \cdot G_M^2(Q^2) + \epsilon \cdot G_E^2(Q^2) = \sigma_T + \epsilon \cdot \sigma_L, \quad (2)$$

where  $\sigma_L$  and  $\sigma_T$  are the cross sections for longitudinally and transversely polarized virtual photons, respectively.

The linear  $\epsilon$  dependence of the cross section is due to the  $\sigma_L$  term. The ratio  $\sigma_L/\sigma_T$  is the so-called Rosenbluth slope related to  $G_E/G_M$  (in OPE), see Fig. 1. The data show that at  $Q^2$  of 4-5 (GeV/c)<sup>2</sup> the Rosenbluth slope is three to four times larger than expected in OPE (shown as the dot-dashed line in Fig. 1) for the observed values of the  $G_E^p/G_M^p$  ratio.

The nucleon electromagnetic form factors can reveal a lot of information about the nucleon internal structure, as well as the quark distribution. The form factors depend only on one variable, the negative square of the four-momentum transfer carried by the photon,  $Q^2$ . In

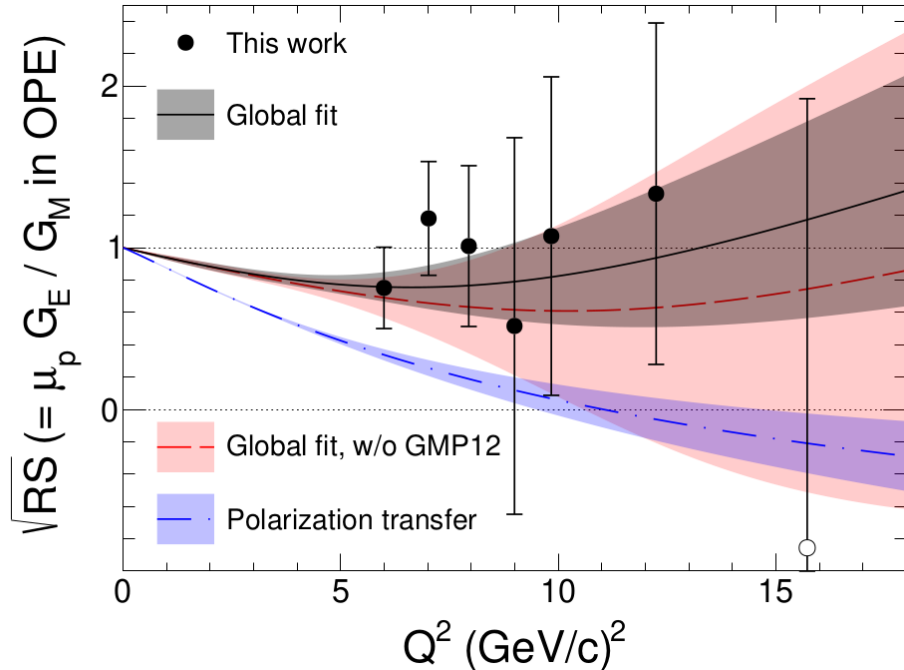


FIG. 1. The square root of Rosenbluth slope, corrected for kinematical factor  $\sqrt{\tau}$  and  $\mu_p$ , observed in elastic electron-proton scattering, adopted from Ref. [3]. References in the plot are also from Ref. [3]

the limit of large  $Q^2$ , perturbative QCD (pQCD) provides well-motivated predictions for the  $Q^2$ -dependence of the form factors and their ratio. However, it was never predicted at what  $Q^2$  range the pQCD prediction (scaling) will be valid. Studies show that pQCD validity will require a very large  $Q^2$  of  $100 \text{ (GeV/c)}^2$ . It was discovered at JLab, using the double polarization methods, that the proton electric and magnetic form factors behave differently starting at  $Q^2 \approx 1 \text{ (GeV/c)}^2$ .

Experimentally, the nucleon form factors can be measured using one of two techniques: the polarization transfer technique and the Rosenbluth technique. The polarization method examines the polarization transfer from longitudinally polarized electron to the recoiling nucleon and determine the resulting azimuthal asymmetry distribution using a polarimeter. Alternatively, one can use a polarized electron beam and polarized target. In the Rosenbluth method, the electric and magnetic form factors can be separated by making two or more

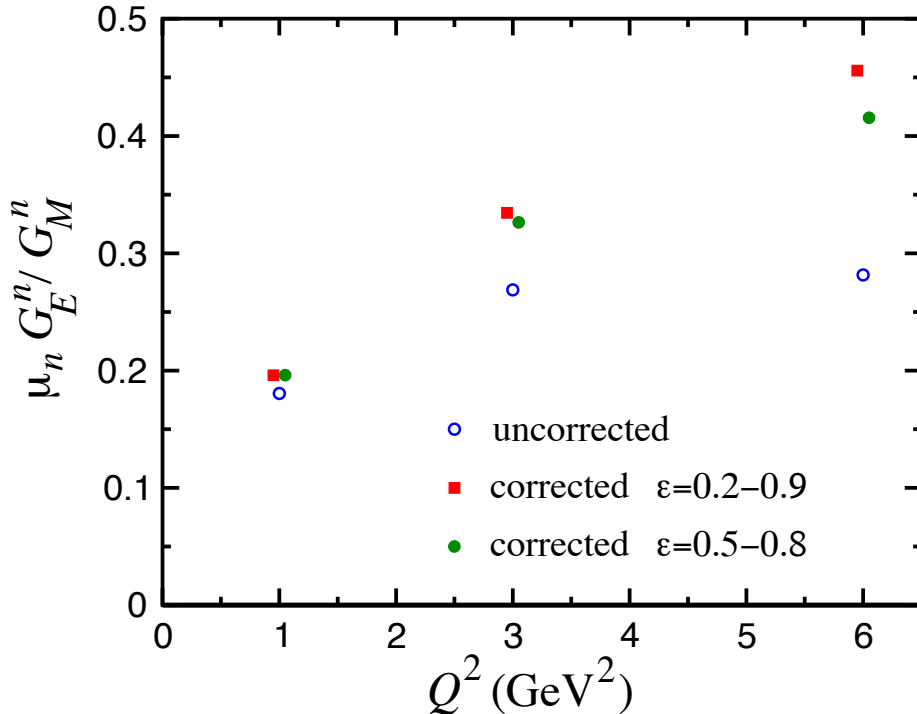


FIG. 2. Projected impact of TPE on  $G_E^n/G_M^n$  using LT separation, according to Ref. [4].

36 measurements with different  $\epsilon$  values (*i.e.* different beam energies and angles), but with same  
 37  $Q^2$  value. The Rosenbluth technique requires an accurate measurement of the cross section  
 38 and suffers from large systematic uncertainties arising from several factors, for instance the  
 39 need for a precise determination of the scattering angle. Additionally, for a measurement  
 40 of the neutron form factors, accurate knowledge of the neutron detector efficiency is re-  
 41 quired, which is particularly hard to achieve. These uncertainties can be greatly reduced by  
 42 measuring the ratio of  $e - n$  and  $e - p$  quasi-elastic cross sections.

43 When comparing the values of  $G_E^p/G_M^p$  obtained from both techniques, a significant dis-  
 44 crepancy was observed (see Fig. 1). Such a discrepancy implies a potential problem in our  
 45 understanding of the nucleon substructure. Many efforts were made to explain this effect,  
 46 and it is believed that the inconsistency is due to the contribution of two-photon exchange in  
 47  $e - N$  elastic scattering process [5, 6]. While the two-photon exchange is currently considered

48 as the most likely explanation for this discrepancy, there is still debate on whether it is the  
49 only source. Fortunately, this contribution is also dependent on the charge of the lepton,  
50 meaning that it will contribute differently to the Rosenbluth slope on  $e^- - N$  and  $e^+ - N$ .

51 Predictions made for the electron-neutron case are shown in Fig. 2, adopted from [4].  
52 Experiment E12-20-010 (currently under analysis) measured for the first time the Rosenbluth  
53 slope in  $e^- - n$ . that a similar measurement as E12-20-010 [7] on positron neutron scattering  
54 is expected to give a different slope.

55

## II. PHYSICS MOTIVATION

56

### A. Form factor measurements at high $Q^2$

57     The nucleon plays the same central role in hadronic physics that the hydrogen atom does  
 58     in atomic physics and the deuteron in the physics of nuclei. The structure of the nucleon  
 59     and its specific properties, such as charge, magnetic moment, size, mass; the elastic electron  
 60     scattering form factors, resonances; and structure functions in DIS, are of fundamental sci-  
 61     entific interest. The isospin is a fundamental property of the nucleon, so both the proton  
 62     and neutron investigations are important to do. By using data on the proton and neutron  
 63     form factors the flavour structure could be explored [8]. It has already provided the most  
 64     direct evidence for a diquark correlation in the nucleon [9–11].

65     Hadron structure, as seen in elastic electron scattering, in one-photon approximation, is  
 66     defined by two functions of four momentum transfer square. They are: the helicity con-  
 67     serving Dirac form factor,  $F_1$ , which describes the distribution of the electric charge, and  
 68     the helicity non-conserving Pauli form factor,  $F_2$ , which describes the distribution of the  
 69     magnetic moment. These two form factors are the ingredients of the hadronic current. They  
 70     contain information on the transverse charge distribution for an unpolarized and transversely  
 71     polarized nucleon, respectively, in the infinite momentum frame [12, 13].

72     The Sachs form factors,  $G_E$  and  $G_M$ , the ratio of which will be extracted directly from  
 73     the data, are related to  $F_1$  and  $F_2$  by

$$F_1 = \frac{G_E + \tau G_M}{1 + \tau} \quad \text{and} \quad F_2 = \frac{G_M - G_E}{\kappa(1 + \tau)}, \quad (3)$$

74     where  $\kappa$  is the nucleon anomalous magnetic moment.

75     Already twenty-four years ago, an important development in QCD phenomenology has  
 76     been the exploration of the generalized parton distribution (GPD) formalism [14–16], which  
 77     provides relations between inclusive and exclusive observables. The nucleon elastic form  
 78     factors  $F_1$  and  $F_2$  are given by the first moments of the GPDs

$$F_1(t) = \sum_q \int_0^1 H^q(x, \xi, t, \mu) dx \quad \text{and} \quad F_2(t) = \sum_q \int_0^1 E^q(x, \xi, t, \mu) dx, \quad (4)$$

79 where  $H^q$  and  $E^q$  are two of the generalized parton distributions,  $x$  is the standard Bjorken  
 80  $x$ ,  $\xi$  is the “skewness” of the reaction,  $t$  is the four-momentum transferred by the electron,  
 81  $\mu$  is a scale parameter necessary for the evolution over  $Q^2$ , analogous to DIS parton distri-  
 82 butions, and the sum is over all quarks and anti-quarks. GPDs may be accessed through  
 83 processes such as deeply virtual Compton scattering, where the interaction is factorized into  
 84 a hard part with the virtual photon/photon interactions with an individual quark and a soft  
 85 part of the residual system where the GPD information is contained.

86 A fundamental nucleon feature, the spin, is related to GPDs, as shown by X. Ji [15]. The  
 87 moments of GPDs can yield information, according to Ji’s Angular Momentum Sum Rule,  
 88 on the contribution to the nucleon spin from quarks and gluons, including both the quark  
 89 spin and orbital angular momentum.

90 At present, experimental measurements of GPDs are still scarce. Until high  $Q^2$  DVCS  
 91 data becomes available, work has been done to attempt to parameterize these GPDs, which  
 92 rely heavily on data from electromagnetic form factors and parton distributions from DIS as  
 93 constraints [17]. Data at high  $Q^2$  for  $G_E^n$  would contribute significantly in the development  
 94 of these models.

95 As we presented above, nucleon elastic form factors provide important input for the  
 96 modeling of GPDs. At the same time, the measured cross section of elastic  $e - p$  scattering  
 97 at high  $Q^2$  is significantly larger than predicted by Born-approximation calculations [18],  
 98 indicating that TPE effects play a critical role in the high- $Q^2$  region and therefore must be  
 99 well understood before conclusions about GPDs can be drawn.

100

## 101 **B. The role of two-photon exchange in form factors**

102 As we presented above the form factors are important components for the study of the  
 103 nucleon structure. However, the puzzle of the form factor ratio at higher  $Q^2$   $G_E/G_M$  partly  
 104 blurs our understanding of the measurements. Such an observation underlines the importance  
 105 of the understanding of the two-photon exchange for hadron physics.

106 There are two different contributions of the two photon-exchange. The first one is the

<sup>107</sup> “soft” two-photon exchange, where one of the photons energy is very small compared to  
<sup>108</sup> the other, which is usually included in radiative correction calculations such as Mo and  
<sup>109</sup> Tsai [19]. The second one, which is the one we’ve referred to so far in this document, is  
<sup>110</sup> the “hard” two-photon exchange, where both photons have a significant energy. The leading  
<sup>111</sup> order contribution of the two-photon exchange to the elastic lepton-nucleon scattering is  
<sup>112</sup> the interference term between the one-photon amplitude term  $\mathcal{M}_{1\gamma}$  and the two-photon  
<sup>113</sup> amplitude term  $\mathcal{M}_{2\gamma}$ :

$$\sigma_{eN} \propto |\mathcal{M}_{1\gamma}|^2 \pm 2\Re e[\mathcal{M}_{1\gamma}\mathcal{M}_{2\gamma}]. \quad (5)$$

<sup>114</sup> This interference term depends on the cube of the charge of the lepton involved, *i.e.* at first  
<sup>115</sup> order the sign of the two-photon exchange contribution is naively expected to flip from  $e^- - N$   
<sup>116</sup> to  $e^+ - N$ . This means that the respective discrepancies between the Rosenbluth slopes of  
<sup>117</sup>  $e^+ - N$  and  $e^- - N$  and  $G_E/G_M$  from polarization transfer should be of same magnitude,  
<sup>118</sup> but going into different directions. Any significant divergence between the two discrepancies  
<sup>119</sup> would point towards an additional phenomenon contributing to the elastic electron-nucleon  
<sup>120</sup> scattering cross section beyond two-photon exchange. The presented measurements purport  
<sup>121</sup> to measure the Rosenbluth slope in positron-neutron scattering compared to electron-neutron  
<sup>122</sup> scattering.

123

### III. TECHNIQUE

124 This proposal is based on instrumentation, simulation, and analysis development made  
 125 by the GMn/SBS collaboration for the GMn, E12-09-019, experiment [20]. The GMn experi-  
 126 ment is one of several form factor experiments approved by JLab PAC. The SBS spectrometer  
 127 was funded by DOE with large contributions provided by the collaborating institutions from  
 128 USA, Italy, UK, and Canada. The apparatus and DAQ installation will start in 2020 and  
 129 the data taking run is expected to be in summer-fall 2021.

130 The neutron form factors are challenging to be determine experimentally especially be-  
 131 cause there is no free neutron target. However, since deuterium is a loosely coupled system,  
 132 it can be viewed as the sum of a proton target and a neutron target. In fact, quasi-elastic  
 133 scattering from deuterium has been used to extract the neutron magnetic form factor,  $G_M^n$ ,  
 134 at modestly high  $Q^2$  for decades [21, 22] in the single arm ( $e, e'$ ) experiments. However, the  
 135 proton cross section needs to be subtracted by applying a single-arm quasi-elastic electron-  
 136 proton scattering. This “proton-subtraction” technique suffers from a number of systematic  
 137 uncertainties e.g. contributions from inelastic and secondary scattering processes.

138 Many years ago, L. Durand [23] proposed the so-called “ratio-method” based on the  
 139 measurement of both  $D(e, e'n)$  and  $D(e, e'p)$  reactions. In this method, many of the system-  
 140 atic errors are canceled out. Several experiments [24–26] have applied the ratio-method to  
 141 determine the neutron magnetic form factor.

142 The GMn/SBS experiment [20] will take data for elastic  $e - n$  scattering for several  
 143 kinematics with  $Q^2$  from 3.5 up to 13.5  $(\text{GeV}/c)^2$ . We propose to use this method to measure  
 144 the Rosenbluth slope and extract (in OPE approximation) the neutron electric form factor,  
 145  $G_E^n$ , at one value of momentum transfer. In fact, one of the required data points will be taken  
 146 by the GMn experiment, so an additional measurement is needed only for one kinematics.

147 Data will be collected for quasi-elastic electron scattering from deuterium in the process  
 148  $D(e, e'n)p$ . Complementary  $D(e, e'p)n$  data will be taken to calibrate the experiment appa-  
 149 ratus. The current knowledge of the  $e - p$  elastic scattering cross section (obtained in the  
 150 single arm  $H(e, e')p$  and  $H(e, p)e'$  experiments) will be also used for precision determination  
 151 the experiment kinematics.

152 Applying the Rosenbluth technique to measure  $G_E^n$  requires accurate measurement of the  
 153 cross section and suffers from large uncertainties. To overcome this issue, we propose to  
 154 extract the value of  $G_E^n$  from the ratio of quasi-elastic yields,  $R_{n/p}$ , in scattering from a  
 155 deuteron target as follows:

$$R_{n/p} \equiv R_{observed} = \frac{N_{e,e'n}}{N_{e,e'p}} \quad (6)$$

156  $R_{observed}$  needs to be corrected to extract the ratio of e-n/e-p scattering from nucleons:

$$R_{corrected} = f_{corr} \times R_{observed} , \quad (7)$$

157 where the correction factor  $f_{corr}$  takes into account the variation in the hadron efficiencies  
 158 due to changes of the  $e - N$  Jacobian, the radiative corrections, and absorption in path from  
 159 the target to the detector, and small re-scattering correction.

160 In one-photon approximation,  $R_{corrected}$  can be presented as:

$$R_{corrected} = \frac{\sigma_{Mott}^n \cdot (1 + \tau_p)}{\sigma_{Mott}^p \cdot (1 + \tau_n)} \times \frac{\epsilon \sigma_L^n + \sigma_T^n}{\epsilon \sigma_L^p + \sigma_T^p} \quad (8)$$

It is important that the ratio  $R_{Mott} = \frac{\sigma_{Mott}^n \cdot (1 + \tau_p)}{\sigma_{Mott}^p \cdot (1 + \tau_n)}$  could be determine with very high relative accuracy even with modest precision for the beam energy, electron scattering angle, and detector solid angle. Now, let us write the  $R_{corrected}$  at two values of  $\epsilon$  using  $S^{n(p)} = \sigma_L^{n(p)} / \sigma_T^{n(p)}$  as:

$$R_{corrected,\epsilon_1} = \frac{\epsilon_1 \sigma_L^n + \sigma_T^n}{\epsilon_1 \sigma_L^p + \sigma_T^p} \quad R_{corrected,\epsilon_2} = \frac{\epsilon_2 \sigma_L^n + \sigma_T^n}{\epsilon_2 \sigma_L^p + \sigma_T^p}$$

In these two equations there are two unknown variables:  $\sigma_L^n$  and  $\sigma_T^n$ . We remind here that proton and neutron measurements are made simultaneously with the same apparatus. Thanks to this, the dominant contribution to the uncertainty of the Rosenbluth slope of the reduced cross section vs.  $\epsilon$ ,  $S^n = \sigma_L^n / \sigma_T^n$ , will come from the uncertainty of  $S^p$ . At  $Q^2=4.5$  (GeV/c)<sup>2</sup>, according to the global analysis of  $e - p$  cross section [3], the value of  $S^p$  is close to  $1/(\tau \mu_p^2) = 0.087$  with an uncertainty of 0.01. The resulting equation for  $S^n$  is:

$$A = B \times \frac{1 + \epsilon_1 S^n}{1 + \epsilon_2 S^n} \approx B \times (1 + \Delta \epsilon \cdot S^n),$$

<sub>161</sub> with  $\Delta\epsilon = \epsilon_1 - \epsilon_2$ , and where the variable  $A = R_{corrected,\epsilon_1}/R_{corrected,\epsilon_2}$  will be measured  
<sub>162</sub> with statistical precision of 0.1%. Assuming, for this estimate, equal values of  $Q^2$  for two  
<sub>163</sub> kinematics, the  $\tau$  and  $\sigma_T$  for two kinematics are canceled out, and the variable

$$B = (1 + \epsilon_2 S^p)/(1 + \epsilon_1 S^p) \quad (9)$$

<sub>164</sub> For actual small range of  $\epsilon$  and small value of the slope,  $B \approx (1 - \Delta\epsilon \cdot S^p)$ . The value of  
<sub>165</sub>  $B$  will be determined from global proton  $e - p$  data to a precision of  $0.25 \times 0.01$ .

<sub>166</sub> At  $Q^2=4.5$  (GeV/c)<sup>2</sup> the ratio  $\mu_n G_E^n/G_M^n$  is  $0.55 \pm 0.05$  based on polarization transfer data  
<sub>167</sub> which is mostly insensitive to the two-photon exchange, see the 2015 review from Perdrisat  
<sub>168</sub> *et al.* [27]. In the simplest model, the slope  $S^n$  is a sum of the slope due to  $G_E^n/G_M^n$  and the  
<sub>169</sub> neutron two-photon exchange nTPE contribution:

$$S^n = (G_E^n/G_M^n)^2/\tau + \text{nTPE} \quad (10)$$

<sub>170</sub> Without the nTPE contribution, our projected measured slope would be  $S^n = (G_E^n/G_M^n)^2/\tau =$   
<sub>171</sub>  $0.063$ .

<sub>172</sub> If we use the prediction available in [4] which is reproduced on our Fig. 2, nTPE leads  
<sub>173</sub> to increase of the neutron Rosenbluth slope  $S^n$  by a factor 2; Under this assumption, the  
<sub>174</sub> projected measured Rosenbluth slope would now become  $S^n = 0.126$ , and nTPE would then  
<sub>175</sub> be:

$$\text{nTPE} = S^n - (G_E^n/G_M^n)^2/\tau = 0.063. \quad (11)$$

<sub>176</sub> The projected measurement of the neutron two-photon exchange for this experiment is  
<sub>177</sub>  $nTPE = 0.063 \pm 0.012 \pm 0.01$ , where the first uncertainty is due to accuracy of  $G_E^n/G_M^n$  and  
<sub>178</sub> the second one due to projected precision of this experiment. It would be a 4-4.5 sigma  
<sub>179</sub> observation of the two-photon exchange contribution for the neutron.

180

#### IV. PROPOSED MEASUREMENTS

181 We propose to use the same experimental setup of the past E12-09-019/E12-20-010  
 182 experiments. We have two kinematic points at  $Q^2 = 4.5 \text{ (GeV/c)}^2$  at two beam passes  
 183 (4.4 GeV/2 pass and 6.6 GeV/3 pass), and two kinematic points at  $Q^2 = 3.0 \text{ (GeV/c)}^2$  at  
 184 two beam passes (3.3 GeV/1.5 pass and 4.4 GeV/2 pass), obtaining two  $\epsilon$  values for each  
 185  $Q^2$  value. Each of these kinematics will be run with unpolarized positron beams at the max-  
 186 imum intensity available for Hall C, *i.e.* 1  $\mu\text{A}$ . Note that the two kinematic points at  $Q^2 =$   
 187 3.0  $(\text{GeV}/c)^2$  will also be run with electrons at an intensity of 10  $\mu\text{A}$ . (the two kinematic  
 188 points at  $Q^2 = 4.5 \text{ (GeV/c)}^2$  will only need to be run for positrons as the past E12-20-010  
 189 experiment already took those measurements for electron). This will allow us to perform the  
 190 standard Rosenbluth method to obtain (in one-photon approximation) the neutron electric  
 191 and magnetic form factors. In addition, the ratio method (Sec. III), in which the systematic  
 192 errors are greatly reduced, will be implemented to calculate the two photon exchange (TPE)  
 193 contribution. The study of the  $\epsilon$  dependence of the reduced cross section will help examine  
 194 the two photon exchange contribution to the neutron form factor ratio  $G_E^n/G_M^n$ . Table. I  
 195 displays the kinematic settings of the proposed experiment.

Kinematic	$e^+/e^- - I_{beam}$ ( $\mu\text{A}$ )	$Q^2$ $(\text{GeV}/c)^2$	E (GeV)	E' (GeV)	$\theta_{BB}$ degrees	$\theta_{SBS}$ degrees	$\epsilon$
<b>1+</b>	$e^+ (1.0)$	4.5	4.4	2.0	41.9	24.7	0.600
<b>2+</b>	$e^+ (1.0)$	4.5	6.6	4.2	23.3	31.2	0.838
<b>3+</b>	$e^+ (1.0)$	3.0	3.3	1.7	42.8	29.5	0.638
<b>3-</b>	$e^- (10.0)$	3.0	3.3	1.7	42.8	29.5	0.638
<b>4+</b>	$e^+ (1.0)$	3.0	4.4	2.8	28.5	31.2	0.808
<b>4-</b>	$e^- (10.0)$	3.0	4.4	2.8	28.5	31.2	0.808

TABLE I. Kinematic settings of the proposed experiment.

196

## V. EXPERIMENTAL SETUP

197 As illustrated in Fig. 3, this experiment will study electron scattering from a 15 cm long  
 198 liquid Deuterium target held in a vacuum. The scattered electron will be detected in the  
 199 BigBite spectrometer with an upgraded electron detector stack. The neutron arm is arranged  
 200 with a dipole magnet 48D48 (SBS) and a segmented hadron calorimeter HCAL. The whole  
 201 detector package was designed and is being assembled for the GMn, E12-09-019, experiment.

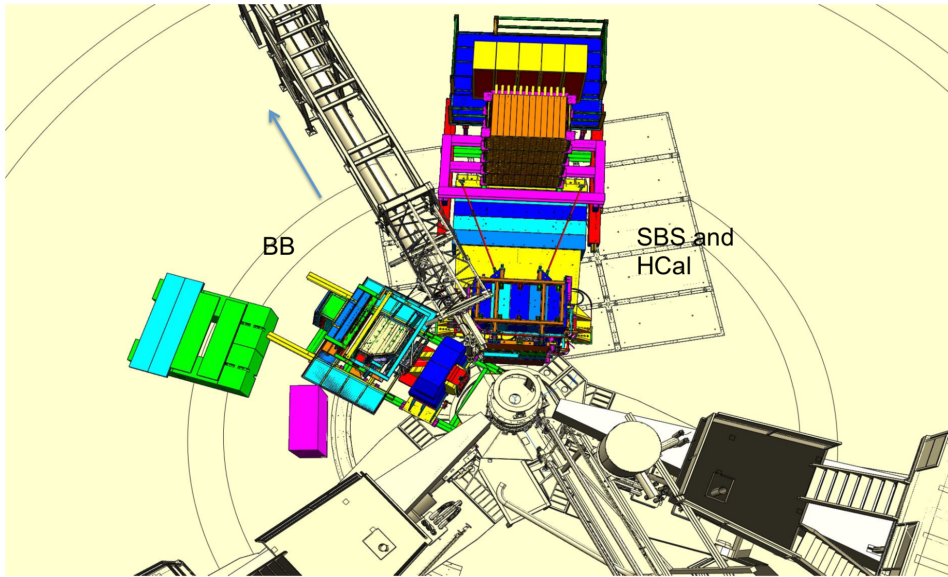


FIG. 3. Layout of the experimental setup in nTPE.

202

### 1. Parameters of the SBS

203 The 48D48 magnet from Brookhaven was acquired as part of the Super Bigbite project  
 204 and will be available for this experiment. It consists of a large dipole magnet which provides  
 205 a field integral of about  $1.7 \text{ T} \cdot \text{m}$ , allowing for quasielastic protons to be sufficiently deflected  
 206 to allow clear differentiation from neutrons. The active field volume has an opening of  $46 \times$   
 207  $25 \text{ vertical} \times \text{horizontal}$ ), matching the aspect ratio of the neutron arm, and a depth of 48  
 208 cm.

209 The placement of this magnet will be 1.6 m away from the target, which would normally

210 interfere with the beamline. To accommodate this, modifications were made to the iron yoke  
211 such that the beamline will pass through the magnet yoke area.

212 The field configuration will be such that positively charged particles will be deflected  
213 upwards away from the hall floor. For a field integral of 1.7 Tesla-m, protons of momentum  
214 2.5 GeV/c will be deflected 250 mrad, which translates to a displacement of 1.29 m. Including  
215 expected detector resolution, the  $p_{miss,\perp}$  distribution will be similar to what was seen in  
216 E02-013, so cuts of < 100 MeV/c will be appropriate. Monte Carlo simulations show a  
217 contamination of charged quasielastics to be negligible.

218 The presence of the magnet also works to sweep low energy charged particles from the  
219 target away from the neutron arm. Particles of momentum less than 1.3 GeV/c will be  
220 entirely swept outside of the neutron arm acceptance. This greatly reduces the amount of  
221 charged low energy background.

222

### A. The BigBite Spectrometer

223 Scattered electrons will be detected in the BigBite spectrometer. The spectrometer con-  
 224 sists of a single dipole magnet (with magnetic field approximately 1.2 T) and a detection  
 225 system, see Fig. 4.

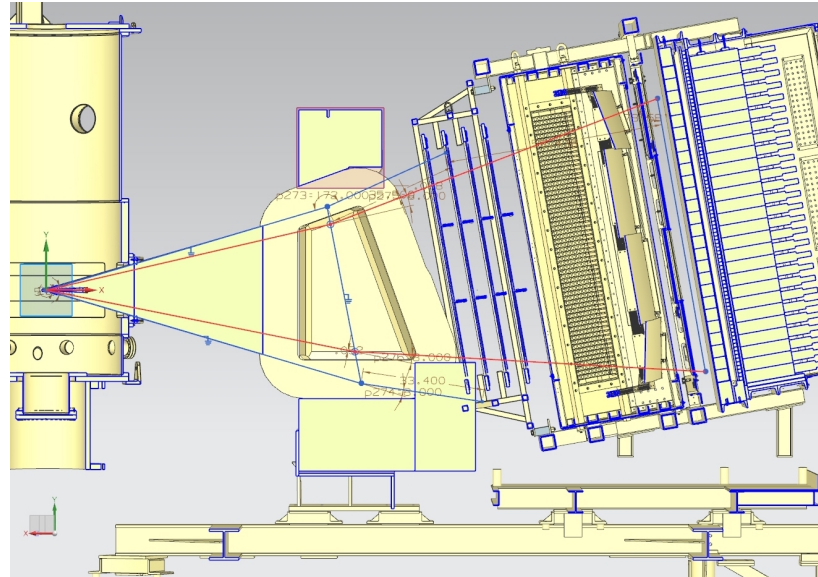


FIG. 4. The BigBite spectrometer with the upgraded detector stack.

226

#### 1. GEM Chambers

227 To perform the tracking of charged particles under the high rates anticipated for this  
 228 experiment, the drift chambers were replaced with gas electron multiplier (GEM) detectors.  
 229 These detectors have proven to be capable of operating under luminosities of  $25 \text{ kHz/mm}^2$   
 230 for the COMPASS experiment at CERN and the spatial resolution of each of these chambers  
 231 is anticipated to be about  $70 \mu\text{m}$ . There will be two sets of GEMs placed on each side of the  
 232 GRINCH Cherenkov detector.

233 The set of GEMs in front of the GRINCH is composed of four layers of GEMs. Two of  
 234 these layers have been built by the SBS collaborators from INFN. They are composed three

235 modules each, measuring  $40 \times 50 \text{ cm}^2$ , such that each layer covers  $40 \times 150 \text{ cm}^2$  (the  
236 long dimension being vertical, along the dispersive direction). The readout of these modules  
237 are oriented in the  $x/y$  direction *i.e.* parallel and perpendicular to the dispersive direction  
238 (horizontal and vertical). The two other layers are being built by the SBS collaborators from  
239 UVA. They are composed of a single module measuring  $40 \times 150 \text{ cm}^2$ , the long dimension  
240 again being vertical and along the dispersive direction. The readout of these modules are  
241 oriented in the  $u/v$  direction *i.e.*  $\pm 30$  degrees with respect to the horizontal direction.

242 The set of GEMs behind the GRINCH has been built by the SBS collaborators from  
243 UVA. It is composed of a single layer composed of four modules measuring  $50 \times 60 \text{ cm}^2$ ,  
244 such that the layer covers  $60 \times 200 \text{ cm}^2$  (the long dimension again being along the dispersive  
245 direction). The readout of these modules are all oriented in the  $x/y$  direction.

246 The background levels in the GEMs have been evaluated, with the help of the G4SBS  
247 simulation package([28] and Sec. VI) for the  $G_M^n$  experimental readiness review. For the  
248  $G_M^n$  highest  $Q^2$  point (which is the most constraining, since it combines mandatory maxi-  
249 mum luminosity and smaller BigBite angles), the rates in the front GEMs are of the order  
250 of  $120 \text{ kHz/cm}^2$  for the front GEM layers, and below  $50 \text{ kHz/cm}^2$  for the back GEM. To  
251 perform the GEM tracking within such a high-rate environment, we use the cluster recon-  
252 structed in the BigBite shower as a track seed to clean the large combinatorics that would  
253 otherwise be created by the large number of hits. After this, the main challenge is the  
254 separation by the clustering algorithm of the signal and background hits to minimize track  
255 smearing. At this level of background, a TreeSearch tracking algorithm combined with a  
256 fairly simple cluster separation algorithm has already proven to achieve 70% efficiency at  
257 nominal luminosity. A better cluster separation algorithm is currently being developed and  
258 should allow to significantly improve this figure.

259 *2. Shower/Preshower*

260 The electromagnetic calorimeter configuration consists of two planes of lead glass blocks  
261 which we call the preshower and shower. The preshower, located about 80 cm behind the  
262 first GEM chamber, consists of a  $2 \times 26$  plane of  $37 \text{ cm} \times 9 \text{ cm}$  blocks. The shower, about

<sup>263</sup> 1 m behind the first GEM chamber, consists of an  $7 \times 27$  array of 8.5 cm  $\times$  8.5 cm blocks.  
<sup>264</sup> Sums over these blocks form the physics event trigger for the experiment.

<sup>265</sup> The preshower signal can be used to provide an additional method of pion rejection.  
<sup>266</sup> By selecting low preshower signals, a pion rejection factor of 1:50 can be achieved through  
<sup>267</sup> optimization. Despite higher particle rates, pion rejection performance is anticipated to  
<sup>268</sup> be similar to that achieved for Transversity, E06-010. By measuring the pedestal widths  
<sup>269</sup> and resolution for E06-010 and scaling to this proposal's conditions, overall relative energy  
<sup>270</sup> resolution for the detector is expected to become worse by a factor of 1.6, to about  $\sigma_{\delta E/E} =$   
<sup>271</sup> 25%.

<sup>272</sup> *3. Timing hodoscope*

<sup>273</sup> The BigBite timing hodoscope has been built by the SBS collaborators from Glasgow to  
<sup>274</sup> replace the BigBite scintillator plane. It will be composed of 90 bars stacked in a plane,  
<sup>275</sup> each with dimensions 1 in.  $\times$  1 in.  $\times$  60 cm. The paddle stack will be oriented such that  
<sup>276</sup> the long dimension of the bars is horizontal *i.e.* perpendicular to the dispersive direction.  
<sup>277</sup> Each of these elements are read out by a PMT on each side, mostly to provide measurement  
<sup>278</sup> redundancy.

<sup>279</sup> This plane will primarily be used to provide a signal for nucleon time of flight reconstruc-  
<sup>280</sup> tion. A time resolution of 200 ps is anticipated. This fine segmentation is meant to lower the  
<sup>281</sup> rates in the detector. Background studies made for the  $G_M^n$  experimental readiness review  
<sup>282</sup> demonstrated that the rates experienced by each element was  $\leq$  500 kHz at a luminosity of  
<sup>283</sup>  $2.8 \times 10^{38}$  cm $^{-2}$  s $^{-2}$ . Signals from the PMTs are processed by NINO front-end cards which,  
<sup>284</sup> when the PMT pulse crosses the NINO threshold, will produce a digital signal to be read  
<sup>285</sup> out by CAEN 1190 TDCs which record a leading time and a trailing time.

<sup>286</sup> *4. GRINCH cherenkov detector*

<sup>287</sup> The main purpose of the GRINCH is to provide additional particle identification for offline  
<sup>288</sup> pion rejection. The GRINCH consists of a tank with a maximum depth of 88.9 cm, with 4

<sup>289</sup> cylindrical mirrors focusing the cherenkov light directly onto a 510 PMT array (60 lines of  
<sup>290</sup> PMTs, with lines of 9 PMTs alternating with lines of 8 PMTs) placed away from the beam.  
<sup>291</sup> The radiation gas will be  $C_4F_8$ , which is by far the best compromise between light yield  
<sup>292</sup> for electrons and operating cost. With  $n - 1 = 1.35 \times 10^{-3}$ , the  $\pi$  threshold is only about  
<sup>293</sup> 2.7 GeV, so the additional pion rejection will be most effective below this threshold.

<sup>294</sup> Similar to the timing hodoscope, the signals from the GRINCH PMTs pulses are processed  
<sup>295</sup> by NINO front-end cards which, when the PMT pulse crosses the NINO threshold, will  
<sup>296</sup> produce a digital signal to be readout by VETROC TDCs, which for each PMT hit will  
<sup>297</sup> record a leading time and a trailing time. The analog signal will not be recorded however,  
<sup>298</sup> which means that for each PMT hit, the information of the number of photoelectrons is not  
<sup>299</sup> directly available (although it can in theory be deduced from the time over threshold).

<sup>300</sup> All of this implies that the electron selection relies on the number of GRINCH PMT  
<sup>301</sup> firing, instead of relying on the signal amplitude.

302

## B. Hadron Calorimeter (HCal)

303

### 1. Description

304 The Hadron Calorimeter (HCal) has been designed specifically to measure the recoil  
 305 nucleon for the SBS experiments. Specifically for this experiment (and for  $G_M^n$ ), HCal  
 306 combined with the SBS (48D48) magnet provides identification of the recoil nucleon, as  
 307 well as additional kinematic constraint and possibly timing information on the measured  
 308 interaction. Nucleon identification is illustrated on Fig. 5. This figure shows the compared  
 309 proton and neutron position distribution in HCal at the same electron kinematics. The  
 310 proton distribution is being shifted upwards by about 1 m compared to the neutron.

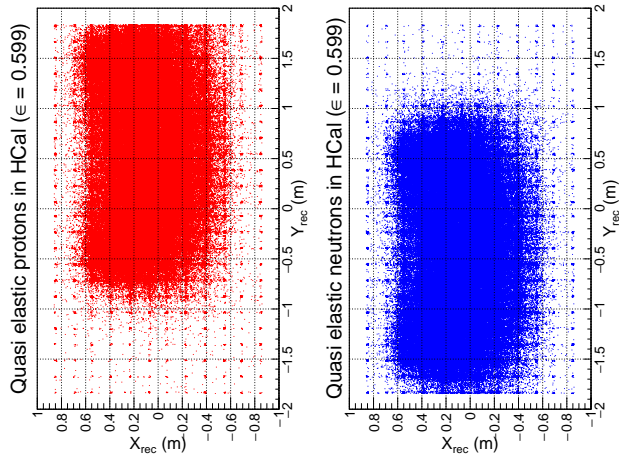


FIG. 5. Reconstructed HCal cluster from quasi-elastic events generated by G4SBS. The left distribution in red is for the proton, the right distribution in blue is for the neutron.

311

The HCal (a CAD model of which is shown in Fig. 6) is composed of 288 modules arranged  
 312 in an array of  $12 \times 24$ . In front of the full assembly is located a  $3/4$  – inch steel plate which  
 314 serves two purposes:

315

- initiate the hadronic shower to optimize the calorimeter response;
- shield the modules from a fraction of the low energy secondaries;

316

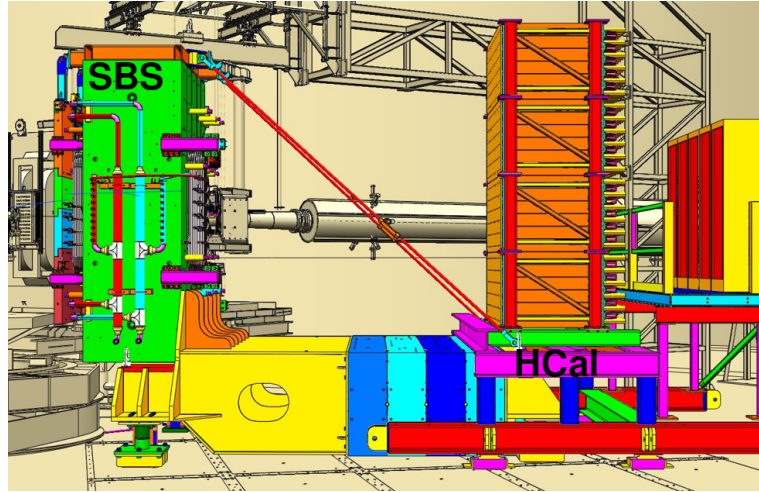


FIG. 6. CAD representation of HCal (right) with the SBS magnet (left)

317 Each of these modules measures  $6 \times 6 \text{ in}^2$  section, for 3 ft length. They are composed of  
 318 alternating tiles of scintillators and iron around a central light guide which collects the light  
 319 generated in the scintillators by the hadronic shower, and guides it to the PMT at the end of  
 320 the block. Cosmic tests have determined that the average light yield for the HCal modules  
 321 is around 5 photoelectrons per MeV deposited in the scintillator tiles.

322 The PMTs are read out with FADC250 which sample the PMT signal every 4 ns and  
 323 allow to reconstruct the PMT pulse shape, and hence its timing. They are also read out by  
 324 TDCs which provide additional timing information. Thanks to this, the timing resolution  
 325 can be better than 1 ns, which cosmic tests (in progress) seem to confirm.

326 The energy resolution is intrinsically broad (see Fig. 12 in Section VI), due mostly to the  
 327 small fraction of energy from the hadronic shower actually measured by the scintillator tiles  
 328 ( $\leq 0.1$  - refer yet again to Fig. 12).

329

## 2. Discussion on HCal efficiency

330 A crucial parameter of this experiment is the hadron calorimeter efficiency, which is  
 331 expected to be slightly different for protons and neutrons, and more importantly the efficiency  
 332 stability.

<sup>333</sup>      *a. Experimental evaluation of HCal efficiency* The calorimeter efficiency will be mea-  
<sup>334</sup>      sured by using "elastic" reactions  $H(e, e')p$ ,  $H(\gamma, \pi^+)n$  and more with  $D(\gamma, \pi^+)n$  and  
<sup>335</sup>       $D(\gamma, \pi^-)p$  single pion production. Fig. 7 (a) shows the projected proton position from  
<sup>336</sup>       $H(e, e')p$ , Fig. 7 (b) shows the projected proton position from  $H(\gamma, \pi^+)n$ . In each case, the

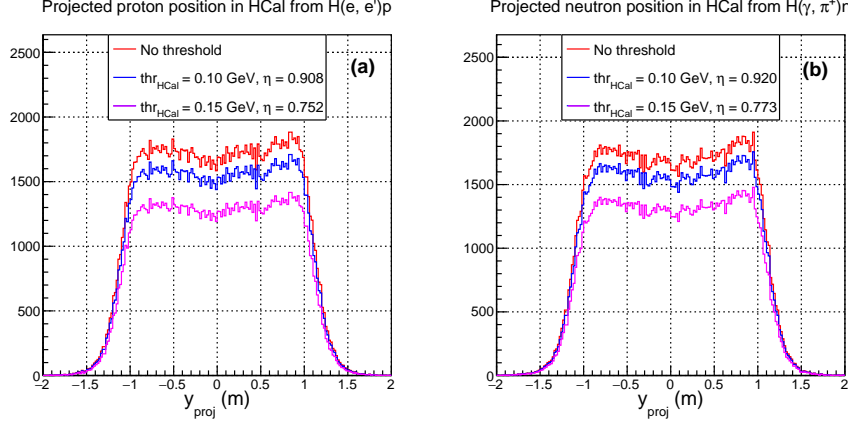


FIG. 7. Projected position in HCal in for the protons in  $H(e, e')p$  (a) and the neutrons in  $H(\gamma, \pi^+)n$  (b). On both panels, red distributions show the projected distribution for  $p, n$ , not detected; blue distributions show the distribution for  $p, n$  detected with a 0.1 GeV threshold; magenta distributions show the distribution for  $p, n$  detected with a 0.15 GeV threshold.

<sup>337</sup>  
<sup>338</sup> trigger will not use the nucleon detector information. Blue distributions on Fig. 7 show the  
<sup>339</sup> expected Y distribution applying a 0.10 GeV threshold on HCal; Magenta distributions on  
<sup>340</sup> Fig. 7 show the expected Y distribution applying a 0.15 GeV threshold on HCal. As re-  
<sup>341</sup> ported in the E12-09-019 GMn proposal [20] on Table 8, the expected recorded statistics for  
<sup>342</sup>  $H(\gamma, \pi^+)n$  are of the order of 4000 events, which will represent a relative 1.5% uncertainty on  
<sup>343</sup> the neutron efficiency. The recorded statistics for  $H(e, e')p$  are of the order of 82000 events,  
<sup>344</sup> which will represent a relative 0.3% uncertainty on the proton efficiency.

<sup>346</sup>

<sup>347</sup>      *b. Impact of efficiency ratio on the neutron / proton yields ratio*      We want to eval-  
<sup>348</sup> uate the impact of the ratio of hadron efficiencies,

<sup>349</sup>       $R_{\eta_n/p} = \eta_n/\eta_p$  on the ratio of neutrons to proton yields  $R_{n/p} = N_{en}/N_{ep}$ .

<sup>350</sup>      To obtain the "true" ratio of neutrons to proton yields  $R_{n/p}$  from the recorded "raw"

<sup>351</sup> ratio of neutrons to proton yields  $R_{n/p,raw}$ , this ratio needs to be corrected by  $R_{n/p}$ .

$$R_{n/p} = R_{n/p,raw}/R_{\eta_{n/p}} \quad (12)$$

<sup>352</sup> Hence, the uncertainty,  $\Delta R_{n/p}$  of  $R_{n/p}$  could be expressed as:

$$\Delta R_{n/p}/R_{n/p} = \Delta R_{\eta_{n/p}}/R_{\eta_{n/p}}. \quad (13)$$

<sup>353</sup> To evaluate the uncertainty of  $R_{\eta_{n/p}} = \eta_p/\eta_n$ , we need to account for the strong correlation  
<sup>354</sup> between  $\eta_p$  and  $\eta_n$ ,  $\rho_{\eta_{n/p}}$ . We can define the covariance between the uncertainties  $\Delta\eta_p$  and  
<sup>355</sup>  $\Delta\eta_n$ ,  $\sigma_{\eta_{n/p}} = \rho_{\eta_{n/p}}\Delta\eta_n\Delta\eta_p$ .

<sup>356</sup> We can write the uncertainty on the ratio efficiencies:

$$\frac{\Delta R_{\eta_{n/p}}}{R_{\eta_{n/p}}} = \sqrt{\left(\frac{\Delta\eta_n}{\eta_n}\right)^2 + \left(\frac{\Delta\eta_p}{\eta_p}\right)^2 - 2\frac{\sigma_{\eta_{n/p}}}{\eta_n\eta_p}} \quad (14)$$

$$= \sqrt{\left(\frac{\Delta\eta_n}{\eta_n}\right)^2 + \left(\frac{\Delta\eta_p}{\eta_p}\right)^2 - 2\frac{\rho_{\eta_{n/p}}\Delta\eta_n\Delta\eta_p}{\eta_n\eta_p}} \quad (15)$$

<sup>357</sup>  $\Delta\eta_p$  and  $\Delta\eta_n$  are the uncertainties from the calibration measurements described above. The

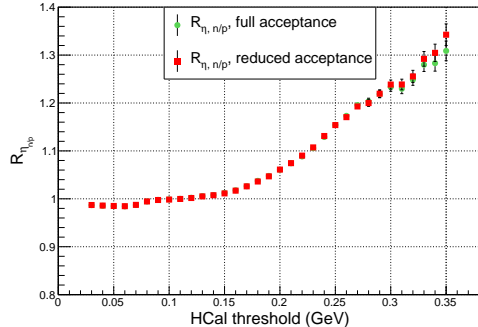


FIG. 8. Neutron/proton efficiency ratio  $R_{\eta_{n/p}}$  as a function of the calorimeter threshold, for our quasi-elastic sample. The error bars represent the uncertainty from the calibration measurements discussed earlier. The green represents  $R_{\eta_{n/p}}$  on the full acceptance, the red represents  $R_{\eta_{n/p}}$  on a reduced acceptance.

<sup>358</sup>

<sup>359</sup>

<sup>360</sup> correlation between the variations of the proton and neutron efficiencies  $\rho_{\eta_{n/p}}$ , depends on

<sup>361</sup> the cause of the variations. In the case of the efficiency calibrations runs, discussed in the  
<sup>362</sup> Monday write-up, the uncertainties of the efficiencies are due to the statistic of the collected  
<sup>363</sup> events. In such a case,  $\rho_{\eta_{n/p}} = 0$ . However, in the case of the detector instability,  $\rho_{\eta_{n/p}} \sim 1$   
<sup>364</sup> (see again Fig. 8).

<sup>365</sup> With the statistics projected for the calibration runs:  $\eta_p \pm \Delta\eta_p = 0.915 \pm 0.003$  and  
<sup>366</sup>  $\eta_n \pm \Delta\eta_n = 0.924 \pm 0.014$ . Applying these values to Eq. 15, the relative uncertainty on the  
<sup>367</sup> absolute value of the hadron efficiency ratio becomes:

$$\Delta R_{\eta_{n/p}}/R_{\eta_{n/p}} = 1.6\%. \quad (16)$$

<sup>368</sup> Considering  $R_{\eta_{n/p}} = 0.991$  from Fig. 8,  $\Delta R_{\eta_{n/p}}/R_{\eta_{n/p}} = 0.016$ . This would add up to the total  
<sup>369</sup> systematic uncertainty of  $R_{n/p}$  to 1.9% for the low  $\epsilon$  kinematic and to 1.6% for the high  $\epsilon$   
<sup>370</sup> kinematic.

<sup>371</sup>

<sup>372</sup> However, the measurement of the Rosenbluth slope,  $S^n = \sigma_L/\sigma_T$ , is unaffected by the  
<sup>373</sup> uncertainty of the absolute value of the efficiency ratio  $R_{\eta_{n/p}}$ .  $R_{\eta_{n/p}}$  will be cancelled in the  
<sup>374</sup> the determination of the neutron Rosenbluth slope  $S^n$ , *as long as we control the stability of*  
<sup>375</sup>  *$R_{\eta_{n/p}}$  over the few days of the measurement.*

<sup>376</sup> c. *Impact of efficiency stability on the Rosenbluth slope measurement* The specific  
<sup>377</sup> value of the hadron calorimeter efficiency does not impact the quality of the experimental  
<sup>378</sup> result. However, the stability of the efficiency ratio is essential.

<sup>379</sup> Let us evaluate in detail the influence of the hadron efficiencies,  $\eta_n$  and  $\eta_p$ , on the exper-  
<sup>380</sup>imental result. The  $S^n$  result is sensitive only to the ratio of neutron efficiency to proton  
<sup>381</sup>efficiency,  $R_\eta = \eta_n/\eta_p$ . Such a ratio is very stable because the nucleon momenta are the  
<sup>382</sup>same by definition of the Rosenbluth method. We have a plan to monitor the stability of  
<sup>383</sup>this ratio in our experimental data.

<sup>384</sup> Our primary experimental observable is the ratio of yields  $R_{n/p} = N_{en}/N_{ep}$ . In this  
<sup>385</sup>experiment, the parameter of interest is  $A = [R_{n/p,\epsilon-1}/R_{n/p,\epsilon-2}] \times [R_{\eta,epsilon-1}/R_{\eta,epsilon-2}]$ .

<sup>386</sup> As we wrote in our proposal, pages 12 and 13, and under the assumption that the reduced

<sup>387</sup> cross section  $\sigma_R$  is linear in  $\epsilon$ , the neutron Rosenbluth slope  $S^n$  can be obtained as:

$$S^n = \frac{A - 1}{\Delta\epsilon} + S^p = \left( \frac{R_{n/p,\epsilon-1}}{R_{n/p,\epsilon-2}} \times \frac{R_{\eta,epsilon-1}}{R_{\eta,epsilon-2}} - 1 \right) / \Delta\epsilon + S^p \quad (17)$$

<sup>388</sup> As it is easy to see from the formula above, the efficiency impact cancels out in  $S^n$  if the  
<sup>389</sup> efficiency ratio is stable.

<sup>390</sup> The procedure to evaluate the hadron detector efficiency was described above. The result  
<sup>391</sup> will be fitted by a few parameter functions, and the ratio of efficiency  $R_\eta$  is characterized  
<sup>392</sup> by those parameters as well as the threshold. This study will be performed for all modules  
<sup>393</sup> of HCal used in the experiment. After the data collection, we will repeat this study with  
<sup>394</sup> the recorded data for each kinematic. Based on projected statistics of a few million events,  
<sup>395</sup> the accuracy of  $R_\eta$  will be better than 0.1%. With such an accuracy, we will monitor the  
<sup>396</sup> stability of  $R_\eta$ . This corresponds to the uncertainty in  $S^n$ , using the formula above, of 0.004,  
<sup>397</sup> with our  $\Delta\epsilon = 0.24$ .

<sup>398</sup> Additional analysis of the efficiency ratio is presented on Fig 8. This analysis focused on  
<sup>399</sup> absolute value of efficiency ratio, for which we expect 1% statistical level. To monitor the  
<sup>400</sup> stability, we will have hundreds of times more statistics.

<sup>401</sup> *d. Efficiency stability due to the detector parameters drift* As we know, the stability  
<sup>402</sup> of the hadron detector efficiency is critical for a successful measurement. The instability of  
<sup>403</sup> the efficiency  $\eta$  over time is mainly due to the drift of the PMTs signals and the related  
<sup>404</sup> electronics. Such an amplitude drift is typically of 1-2% over a few days. It will be better  
<sup>405</sup> for our detector thanks to the LED calibration system.

<sup>406</sup> We expect to use a threshold  $A_{thr} = 100$  MeV (see plots of amplitude spectrum in the  
<sup>407</sup> Monday write-up). Using the graph of the nucleon detection efficiency as a function of the  
<sup>408</sup> threshold  $A_{thr}$  on Fig. 9, we find that, in the region  $A_{thr} = 90 - 110$  MeV, the efficiency is:

$$\eta = 0.92 - 0.18 \times \frac{A[\text{MeV}] - 100}{100} \quad (18)$$

<sup>409</sup> A one percent variation of  $A_{thr}$  leads to 0.2% variation of efficiency.

<sup>411</sup> Turning now to the ratio of efficiencies, we plot it as a function of the threshold on  
<sup>412</sup> Fig. 9. We find that, in the region  $A_{thr} = 90 - 110$  MeV, the ratio of efficiencies is:

$$R_{\eta_n/\eta_p} = \frac{\eta_n}{\eta_p} = 0.998 + 0.011 \times \frac{A[\text{MeV}] - 100}{100}. \quad (19)$$

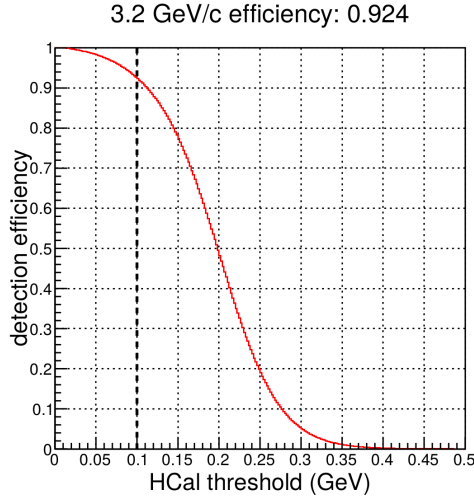


FIG. 9. Nucleon detection efficiency vs the calorimeter threshold  $A_{thr}$ .

- <sup>413</sup> Using the estimate for a PMT-based system instability of 1-2%, which means that  $A_{thr}$  is  
<sup>414</sup> stable to 1-2 MeV, the ratio of efficiencies  $R_{\eta_{n/p}} = \frac{\eta_n}{\eta_p}$  is found to be stable to 0.022%.  
<sup>415</sup> The run plan of the GMn experiment (E12-09-019), which will run next summer, has a  
<sup>416</sup> provision of running on the hydrogen target multiple times with different fields in the SBS  
<sup>417</sup> dipole, allowing the study of the stability of individual modules of HCal.

418      **VI. SIMULATIONS, ESTIMATIONS OF COUNTING RATES AND**  
 419      **ACCIDENTALS**

420      The estimates of counting rates accidentals have been performed using G4SBS, the  
 421      GEANT4-based simulation package developed for the SBS experiment [28]. This package  
 422      includes a wide range of event generators, which allows us to evaluate the rates for both  
 423      events of interest (signal) and background. The representation of the experiment apparatus  
 424      in G4SBS is shown in the high  $\epsilon$  configuration in Fig. 10.

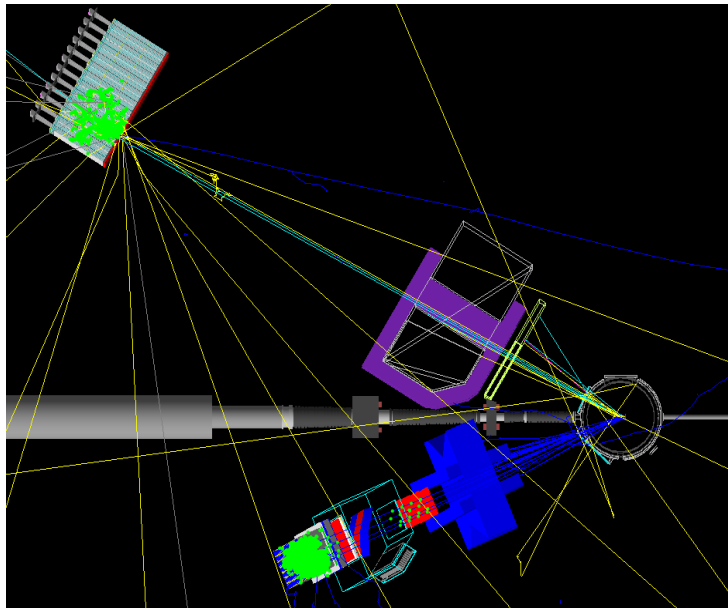


FIG. 10. Top view of the experimental apparatus model in G4SBS, shown in the high  $\epsilon$  configuration. The beam direction is indicated, as well as the main elements (HCal, SBS magnet, BigBite spectrometer)

425      During the development of the NTPE/E12-20-010 proposal, we had run extensive sim-  
 426      ulations to show that the trigger rates were manageable, and that the backgrounds were  
 427      tolerable for the experiment, which was originally planned to run at  $30 \mu\text{A}$ , which is thirty  
 428      (three) times the luminosity of the positron (electron) kinematics for this experiment. Dur-  
 429      ing the NTPE data taking, we effectively run at a lower current of  $5\text{-}15 \mu\text{A}$ , as the GEMs  
 430      were experiencing hardware issues that were limiting their range of operations (please note

431 that these issues have since then been debugged and fixed, and will not be an issue whatso-  
432 ever). Such beam intensities remain well above the beam intensities that are available with  
433 positrons anyway.

434 **A. Background and trigger rates for NTPE/E12-20-010**

435 We present here the trigger rates estimated for NTPE/E12-20-010, which was planned to  
436 run at  $30 \mu\text{A}$ . The main processes expected to contribute to the trigger rates for the BigBite  
437 spectrometer are:

- 438 • the inelastic electron nucleon scattering process;
- 439 • photons from inclusive  $\pi^0$  production;
- 440 • and to a lesser extent, charged pions.

441 Concerning HCal, various hadronic backgrounds are expected to contribute to the rates  
442 in HCal, the dominant ones being pions. Both the inelastic scattering and the inclusive  
443 neutral and charged pion production are implemented in G4SBS, the latter relying on the  
444 Wiser parametrization [29]. The minimum-bias “beam-on-target” generator (including all  
445 electromagnetic and hadronic processes) has also been considered for the HCal background.

446 The thresholds to apply to each arm are determined as a function of the elastic peak. For  
447 the electron arm, the threshold has been set at  $\mu_E - 2.5\sigma_E$ ,  $\mu_E$  and  $\sigma_E$  being respectively  
448 the position and width of the fitted elastic peak. Fig. 11 presents the distributions of rate  
449 of energy deposit for the different processes involved in the BigBite trigger rates.

450 Since HCal is a sampling calorimeter (meaning that only a fraction of the shower energy  
451 is measured), its resolution is relatively wide ( $\sim 0.7$  GeV). Due to this, the threshold is at  
452 90% efficiency (which corresponds to  $\sim 0.1$  GeV for both kinematics. Fig. 12 presents the  
453 distributions of rate of energy deposit for the different processes involved in the HCal trigger  
454 rates.

455 While during the data taking of NTPE(E12-20-010), it was more challenging to set the  
456 BBCal and HCal thresholds exactly as defined above and precisely compare the simulation

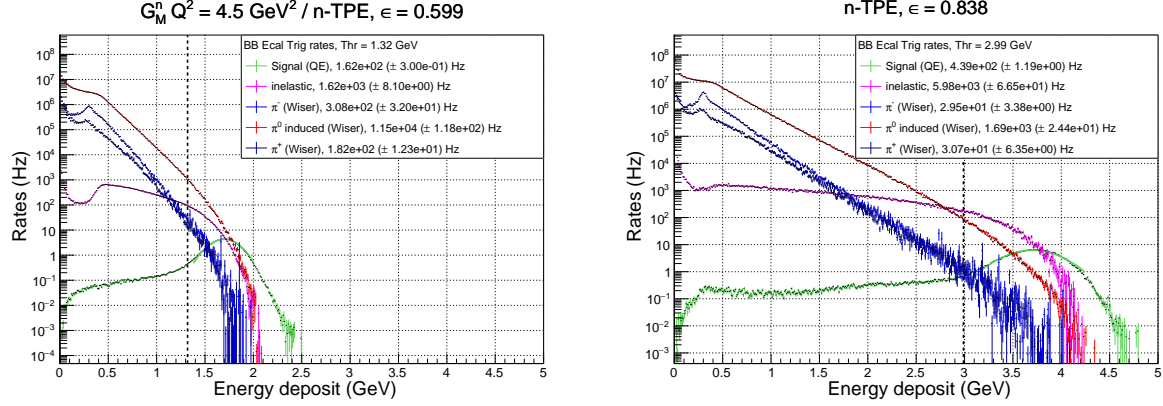


FIG. 11. Rates of the different process contributing to the BigBite electron arm trigger for the original NTPE experiment (E12-20-010), for the low  $\epsilon$  (left) and the high  $\epsilon$  (right). Quasi-elastic is in green, inelastic in magenta,  $\pi^0$  in red,  $\pi^-$  in blue, and  $\pi^+$  in dark blue. Note the resolution for the elastic peak in the BigBite shower is  $\sim 0.3$  GeV. Those rates would be divided by 30 for the positron measurements.

458 with the rates, the observed trigger rates were in the same ballpark as anticipated from the  
 459 simulations, and were not at all a show-stopper at 5-15  $\mu\text{A}$ .

## 460 B. Quasi-elastic counting rates

461 The signals for this experiment have been generated using the G4SBS elastic/quasi-elastic  
 462 generator. We generated a reasonably large sample of quasi-elastic events  $N_{Gen}$  for each  
 463 kinematics, within a solid angle  $\Delta\Omega_{Gen}$  that was larger than the detector acceptance. To  
 464 evaluate the detector solid angle, we define simple criteria that each event has to pass, defined  
 465 as follows:

- 466 • require a primary track, going through all 5 GEM layers (electron arm);
- 467 • require non-zero energy deposit in both the preshower and shower (electron arm);
- 468 • require non-zero energy deposit in HCal (hadron arm).

469 The quasi-elastic data rates and statistics are compiled for both kinematics in Table. II,

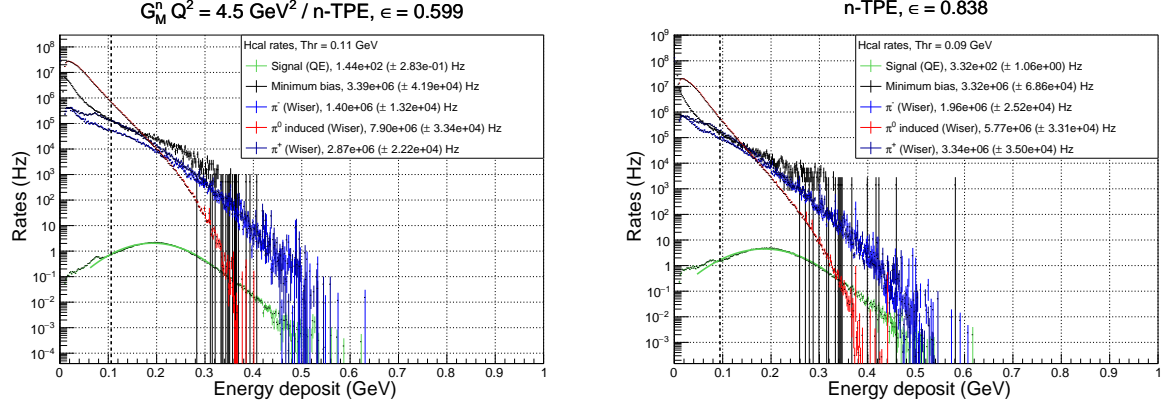


FIG. 12. Rates of the different process contributing to the HCal trigger for the original NTPE experiment (E12-20-010), for the low  $\epsilon$  (left) and the high  $\epsilon$  (right). Quasi-elastic is in green, minimum bias in black,  $\pi^0$  in red,  $\pi^-$  in blue, and  $\pi^+$  in dark blue. Note the peak itself is around 0.2 GeV for 3.2 GeV nucleons. Those rates would be divided by 30 for the positron measurements.

470 along with the respective beam currents, beam/targets, and running times. This table  
 471 includes the measurements on LH2 meant for systematic studies.

472

### C. Projected results

473 The projection for our expected Rosenbluth slope measurement is presented on Fig. 13.  
 474 The projected neutron Rosenbluth slope is based on the estimation of the ratio  $\mu_n G_E^n / G_M^n$  at  
 475  $Q^2=4.5$  (GeV/c)<sup>2</sup> from the 2015 review from Perdrisat *et al.* [27]. This contribution and its  
 476 uncertainty is represented by the blue dashed curve with the blue dotted area on Fig. 17. To  
 477 this contribution is added the two-photon exchange contribution prediction from [4], which  
 478 projects that the two-photon exchange increases the neutron Rosenbluth slope  $S^n$  by a factor  
 479 2. The total Rosenbluth slope is shown as the solid magenta curve on Fig. 17. The projected  
 480 uncertainty on our neutron Rosenbluth slope measurement is represented by the solid black  
 481 curve and error bars with the solid red area. The total uncertainty on the two-photon  
 482 exchange contribution is represented by the magenta dotted area on Fig. 17. It is obtained  
 483 combining the projected uncertainty on the neutron Rosenbluth slope measurement with the  
 484

Point	Beam/ Target	$Q^2$ (GeV/c) $^2$	$E_{beam}$ (GeV)	$I_{beam}$ ( $\mu$ A)	$e - n$ rates (Hz)	$e - p$ rates (Hz)	beam time (h)	$e - n$ counts ( $\times 1000$ )	$e - p$ counts ( $\times 1000$ )
<b>1+</b>	$e^+/\text{LD2}$	4.5	4.4	1.0	0.49	1.54	96	169	532
<b>2+</b>	$e^+/\text{LD2}$	4.5	6.6	1.0	0.94	3.11	48	162	537
<b>3+</b>	$e^+/\text{LD2}$	3.0	3.3	1.0	2.55	7.44	24	220	643
<b>3-</b>	$e^-/\text{LD2}$	3.0	3.3	10.0	25.45	74.45	12	1099	3216
<b>3-</b>	$e^-/\text{LH2}$	3.0	3.3	10.0	-	74.45	12	-	3216
<b>4+</b>	$e^+/\text{LD2}$	3.0	4.4	1.0	4.00	11.67	16	230	672
<b>4-</b>	$e^-/\text{LD2}$	3.0	4.4	10.0	40.00	116.65	8	1152	3360
<b>4-</b>	$e^-/\text{LH2}$	3.0	4.4	10.0	-	116.65	8	-	3360

TABLE II. Quasi-elastic  $e - n$  and  $e - p$  counting rates, for each kinematic, proposed beam-on-target time and total statistics.

485 systematic uncertainty on the uncertainty on the ratio  $\mu_n G_E^n / G_M^n$  at  $Q^2=4.5$  (GeV/c) $^2$ .

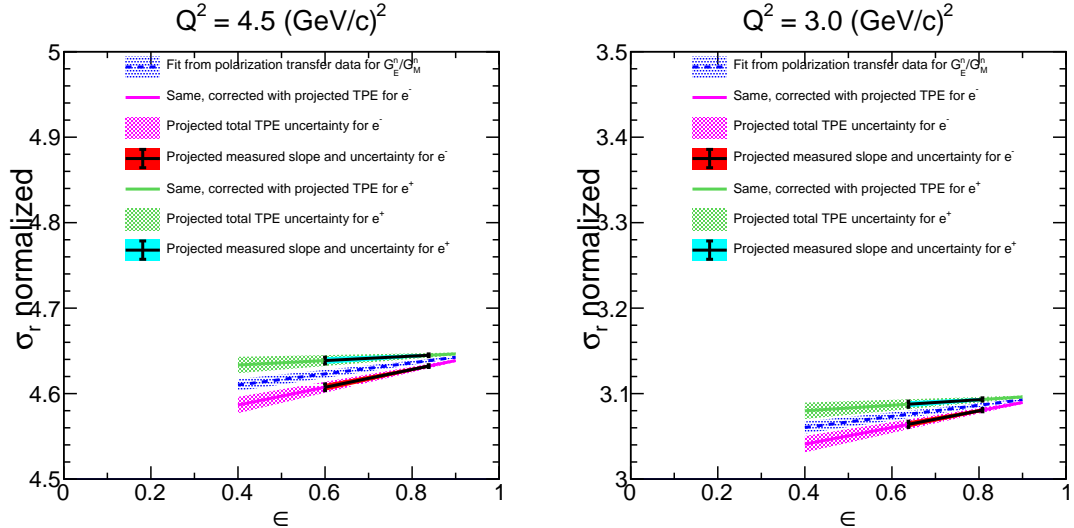


FIG. 13. Projected contribution to the neutron Rosenbluth slope  $S^n$  from  $G_E^n/G_M^n$  (dashed blue curve) with systematic uncertainty (blue dotted area), for  $Q^2 = 4.5 \text{ (GeV/c)}^2$  (left) and  $Q^2 = 3.0 \text{ (GeV/c)}^2$  (right); Total expected neutron Rosenbluth slope  $S^n$  including the expected two-photon exchange for electrons (solid magenta) and positrons (solid green). The constraint that our measurement will bring to the slope is represented in solid black with the solid red area for electrons and cyan area for positron. The magenta and green dotted areas show the total projected uncertainty for nTPE contribution for electrons and positrons.

486

## VII. SYSTEMATIC ERRORS

487 In this section we will estimate (or set upper limits on) the contributions to the sys-  
 488 tematic uncertainty for this experiment. The sources of systematic uncertainties from the  
 489 experimental setup (target, acceptance, inelastic contamination) were already estimated for  
 490 the SBS  $G_M^n$  experiment proposal [20]. Note that a majority of the potential sources of sys-  
 491 tematic uncertainties (nuclear corrections, accidentals, radiative corrections, target density,  
 492 etc) cancel in the ratio  $R = f_{corr} \times N_{e,e'n}/N_{e,e'p}$ , which is one of the strengths of this experi-  
 493 mental method. The sources of uncertainties as well as their estimation for each kinematic  
 494 is provided in Table. III. Since the experimental setup has evolved since then, some of these  
 495 uncertainties have been reevaluated, namely the acceptance loss and inelastic contamination.  
 496 Table. IV lists the estimated contributions to systematic errors on the two-photon-exchange

TABLE III. Estimated contributions (in percent) to the systematic error on  $R = f_{corr} \times N_{e,e'n}/N_{e,e'p}$ . Quantities marked with \* are taken from the SBS  $G_M^n$  experiment proposal [20]. The total systematic errors on  $R$  is the quadratic sum of all other errors.

Kinematic	1+	2+	3+/3-	4+/4-
Acceptance losses	0.5 %	3.0 %	0.6 %	3.2
Inelastic contamination	0.9 %	0.6 %	1.0 %	0.7 %
Nucleon mis-identification*	0.6 %			
Syst. error on $R = f_{corr} \times N_{e,e'n}/N_{e,e'p}$ (Quadratic sum of the errors above)	1.2 %	3.1 %	1.3 %	3.3 %

497

498

500 contribution (TPE). The systematics for  $S^p$  and  $\mu_n G_E^n/G_M^n$  have already been explicated in  
 501 Sec. III, and are the leading contributions to the total uncertainty.

502 To evaluate the upper limit on our uncertainty, we added quadratically the inelastic  
 503 contamination evaluated for the proton and the neutron for each kinematics. This would  
 504 be the error that we make on  $R$  if we ignore the inelastic contamination in the quasi-elastic

TABLE IV. Estimated contributions to systematic error on the Rosenbluth slope.

	$Q^2 = 4.5 \text{ (GeV/c)}^2$	$Q^2 = 3.0 \text{ (GeV/c)}^2$
Syst. error on $p$ cross section ( $S^p = \sigma_L^p / \sigma_T^p$ )	0.01	0.01
Syst. error on $n$ form factor ( $\mu_n G_E^n / G_M^n$ )	0.05	0.041
Syst. error on Rosenbluth slope (TPE)	0.012	0.011

505  $e - n$  and  $e - p$  samples. Even in this case, we expect less than 1% systematic errors. Of  
 506 course, we do plan to reevaluate and subtract the inelastic contamination from our actual  
 507 data sample, so the quoted systematic uncertainty coming from inelastic contamination  
 508 should be a upper limit. In the analysis of NTPE/E12-20-010, the inelastic contamination  
 509 is subtracted from our samples by different methods, which provide very similar results. In  
 510 practice, the systematic from inelastic, while being carefully evaluated, is within the ball  
 511 park of the percent;

512 The acceptance loss in SBS (*i.e.* the proportion of non-detected nucleons for each detected  
 513 electron) have been evaluated for both kinematics. They are about 10% for the  $\epsilon = 0.60$   
 514 kinematic (meaning that for every good electron measured, we will not measure the recoil  
 515 nucleon 10% of the times), but they are over 30 % for the  $\epsilon = 0.84$  kinematics, which is due to  
 516 a larger spread of the nucleon imprint. The systematic uncertainty on the acceptance loss for  
 517 the ratio  $R = f_{corr} \times N_{e,e'n} / N_{e,e'p}$  is maximized by the proton-neutron solid angle asymmetry  
 518  $A_{\Delta\Omega} = \Delta\Omega_n - \Delta\Omega_p / \Delta\Omega_n + \Delta\Omega_p$ . This asymmetry is about 0.5% for the  $\epsilon = 0.60$  kinematic  
 519 (consistent with the  $G_M^n$  proposal), but goes up to 3% for the  $\epsilon = 0.84$  kinematics. In practice,  
 520 in the analysis of NTPE/E12-20-010 this acceptance loss is being alleviated entirely by the  
 521 application of a fiducial cut that rejects all events where either the proton or the neutron  
 522 are out of the acceptance (see Fig. 14.)

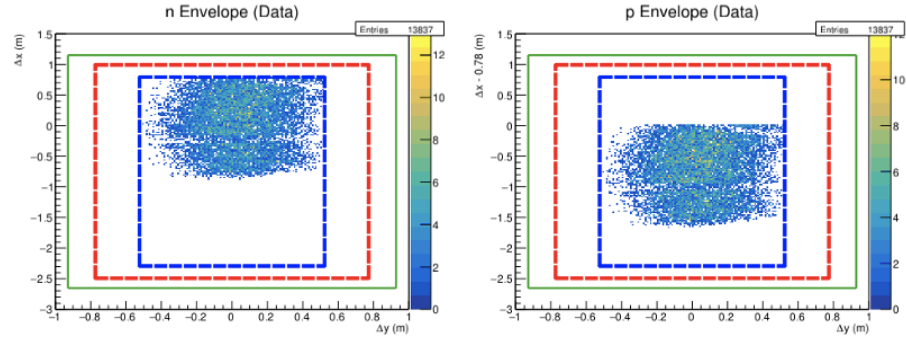


FIG. 14. Fiducial cut applied on the NTPE data: These are the distributions of events projected nucleon position in the HCAL surface. The green limit is the HCal boundary, the red limit is the “active” region, and the blue limit is the fiducial cut, that ensures that we keep the events where both the projected proton and projected neutron are inside the active region.

- 
- 524 [1] R. Hofstadter, *Rev. Mod. Phys.* **28**, 214 (1956).
- 525 [2] M. N. Rosenbluth, *Phys. Rev.* **79**, 615 (1950).
- 526 [3] E. Christy *et al.*, “Two-photon exchange in electron-proton elastic scattering at large four-  
527 momentum transfer,” (2020), in preparation for publication in PRL.
- 528 [4] P. G. Blunden, W. Melnitchouk, and J. A. Tjon, *Phys. Rev.* **C72**, 034612 (2005), arXiv:nucl-  
529 th/0506039 [nucl-th].
- 530 [5] J. Arrington, P. G. Blunden, and W. Melnitchouk, *Prog. Part. Nucl. Phys.* **66**, 782 (2011),  
531 arXiv:1105.0951 [nucl-th].
- 532 [6] A. Afanasev, P. Blunden, D. Hasell, and B. Raue, *Prog. Part. Nucl. Phys.* **95**, 245 (2017),  
533 arXiv:1703.03874 [nucl-ex].
- 534 [7] A. S. W. B. Fuchey, E., “measurement of the two-photon exchange contribution  
535 to the electron-neutron elastic scattering cross section,” See [https://  
536 www.jlab.org/exp\\_prog/proposals/20/PR12-20-010\\_Proposal.pdf](https://www.jlab.org/exp_prog/proposals/20/PR12-20-010_Proposal.pdf)  
537 (2020).
- 538 [8] G. D. Cates, C. W. de Jager, S. Riordan, and B. Wojtsekhowski, *Phys.  
539 Rev. Lett.* **106**, 252003 (2011), arXiv:1103.1808 [nucl-ex].
- 540 [9] C. D. Roberts, M. S. Bhagwat, A. Holl, and S. V. Wright, *Eur. Phys. J.  
541 ST* **140**, 53 (2007), arXiv:0802.0217 [nucl-th].
- 542 [10] J. Segovia, I. C. Cloet, C. D. Roberts, and S. M. Schmidt, *Few Body  
543 Syst.* **55**, 1185 (2014), arXiv:1408.2919 [nucl-th].
- 544 [11] B. Wojtsekhowski (2020) arXiv:2001.02190 [nucl-ex].
- 545 [12] G. A. Miller, *Phys. Rev. Lett.* **99**, 112001 (2007), arXiv:0705.2409 [nucl-  
546 th].

- 547 [13] C. E. Carlson and M. Vanderhaeghen, *Phys. Rev. Lett.* **100**, 032004  
 548 (2008), arXiv:0710.0835 [hep-ph].
- 549 [14] D. Muller, D. Robaschik, B. Geyer, F. M. Dittes, and J. Horejsi, *Fortsch.  
 550 Phys.* **42**, 101 (1994), arXiv:hep-ph/9812448 [hep-ph].
- 551 [15] X.-D. Ji, *Phys. Rev. Lett.* **78**, 610 (1997), arXiv:hep-ph/9603249 [hep-  
 552 ph].
- 553 [16] A. V. Radyushkin, *Phys. Lett.* **B380**, 417 (1996), arXiv:hep-ph/9604317  
 554 [hep-ph].
- 555 [17] M. Diehl and P. Kroll, *Eur. Phys. J.* **C73**, 2397 (2013), arXiv:1302.4604  
 556 [hep-ph].
- 557 [18] N. Kivel, (2020), private communications.
- 558 [19] L. W. MO and Y. S. TSAI, *Rev. Mod. Phys.* **41**, 205 (1969).
- 559 [20] J. Annand, R. Gilman, B. Quinn, B. Wojtsekowski, *et al.*, un-  
 560 published. See [https://www.jlab.org/exp\\_prog/proposals/09/  
 561 PR12-09-019.pdf](https://www.jlab.org/exp_prog/proposals/09/PR12-09-019.pdf), [https://www.jlab.org/exp\\_prog/proposals/  
 562 proposal\\_updates/PR12-09-019\\_pac35.pdf](https://www.jlab.org/exp_prog/proposals/proposal_updates/PR12-09-019_pac35.pdf) (2008).
- 563 [21] E. B. Hughes, T. A. Griffy, M. R. Yearian, and R. Hofstadter, *Phys.  
 564 Rev.* **139**, B458 (1965).
- 565 [22] R. G. Arnold *et al.*, *Phys. Rev. Lett.* **61**, 806 (1988).
- 566 [23] L. Durand, *Phys. Rev.* **115**, 1020 (1959).
- 567 [24] E. E. W. Bruins *et al.*, *Phys. Rev. Lett.* **75**, 21 (1995).
- 568 [25] G. Kubon *et al.*, *Phys. Lett.* **B524**, 26 (2002), arXiv:nucl-ex/0107016  
 569 [nucl-ex].

- 570 [26] J. Lachniet *et al.* (CLAS), Phys. Rev. Lett. **102**, 192001 (2009),  
571 arXiv:0811.1716 [nucl-ex].
- 572 [27] V. Punjabi, C. F. Perdrisat, M. K. Jones, E. J. Brash, and C. E. Carlson,  
573 Eur. Phys. J. **A51**, 79 (2015), arXiv:1503.01452 [nucl-ex].
- 574 [28] A. Puckett, unpublished. See [https://hallaweb.jlab.org/wiki/index.php/Documentation\\_of\\_g4sbs](https://hallaweb.jlab.org/wiki/index.php/Documentation_of_g4sbs) (2016).
- 575 [29] D. E. Wiser, “Photoproduction of protons, kaons and pions at slac en-  
576 ergies,” Ph.D. thesis, University of Wisconsin (1977).